

Neutron- ^{90}Zr mean field from a dispersive optical model analysis

J. P. Delaroche,* Y. Wang, and J. Rapaport

Physics Department, Ohio University, Athens, Ohio 45701

(Received 11 July 1988)

Elastic scattering cross sections have been measured for 8, 10, and 24 MeV neutrons incident on ^{90}Zr . These measurements, together with other neutron elastic scattering and total cross section data available up to 29 MeV, are used in grid searches to obtain an optical model potential which contains a dispersion relation term. This potential is then extrapolated toward negative energies to predict bound single-particle state properties. An overall good description of the data at positive and negative energies is achieved.

I. INTRODUCTION

During recent years, a great deal of theoretical attention has been devoted to casting a proper formulation of the nuclear mean field (NMF) at positive and negative energies.¹ So far, this question has been answered²⁻⁵ with great success for ^{40}Ca and ^{208}Pb , two spherical nuclei often used as testing grounds in structure and reaction studies.

The unified description of the NMF is accomplished using a dispersion relation (DR), which links the real and absorptive terms of the optical model potential (OMP) at positive energies and makes it possible to extrapolate and obtain the main NMF features at negative energies. Usually, this extrapolation is performed adopting either the so-called iterative moment method⁶ or a method based on a dispersive OMP analysis of proton or neutron scattering measurements that need to be available over an energy range as broad as possible. Among these two, by now standard, methods, the last one appears delicate to handle since it deals with many individual best OMP fits which, as is well known, very often provide OMP parameters with values distributed nearly at random over energy.

In the present work, an alternative method based on grid searches for OM potential parameters is suggested and applied to the determination of the nuclear mean field for the neutron- ^{90}Zr system. For that purpose, neutron elastic scattering cross section measurements have been performed at incident energies $E=8, 10, \text{ and } 24$ MeV. These measurements, described in Sec. II, together with earlier neutron scattering⁷⁻¹⁰ and total cross-section^{7,11,12} measurements available in the interval 0.5–29 MeV, and the S - and P -wave strength function values and potential scattering radius,¹³ form the data base considered at positive energies. Section III describes how the grid searches have been conducted. It also includes the DR analysis of the scattering and neutron total cross section measurements. The bound-state properties of the $n+^{90}\text{Zr}$ system are studied in Sec. IV. A discussion is presented in Sec. V and conclusions in Sec. VI.

II. EXPERIMENTAL SETUP AND DATA REDUCTION

The Ohio University beam swinger time-of-flight (TOF) facility¹⁴ was used to measure the neutron elastic scattering differential cross sections $\sigma(\theta)$, from an enriched metallic ^{90}Zr sample at $E=8.0, 10.0, \text{ and } 24.0$ MeV. Monoenergetic 8.0 and 24.0 MeV neutron beams were produced via $T(p,n)^3\text{He}$ and $T(d,n)^4\text{He}$ reactions, respectively. The T_2 gas was contained in a 3 cm long gas cell. A small D_2 contamination in the T_2 gas produced a secondary 10 MeV monoenergetic neutron beam via the $D(d,n)^3\text{He}$ reaction. The incident proton or deuteron beam, pulsed and bunched at a 5 MHz repetition rate with subnanosecond pulse width and with an average beam current of $3 \mu\text{A}$, was incident upon the gas cell. The scattering sample was located at approximately 14 cm from the neutron production source.

Neutrons were detected in a sevenfold array of NE213 liquid scintillation detectors, each of 10 cm thick by 18.8 cm diameter. The flight path from the scattering sample to the neutron detector array was 13 m. Pulse-shape discrimination was used to eliminate γ -ray events in the neutron detectors.

Sample-in and sample-out measurements were normalized to the counting rate of a stilbene scintillator 2.0 cm in diameter by 0.5 cm thick, used as the neutron monitor. This detector was located at 0.82 m from the neutron production target at a fixed angle ($\theta_{\text{lab}}=45^\circ$) relative to the zero-degree line. The obtained energy resolution of the TOF spectrometer were 135, 188, and 410 keV for incident neutrons at 8, 10, and 24 MeV, respectively. Differential scattering cross sections were measured in 3° steps in the $\theta_{\text{lab}}=15^\circ-90^\circ$ interval range and every 5° between $\theta_{\text{lab}}=90^\circ$ and 156° . A complete description of the experimental setup is presented in Ref. 15.

The scattering sample was of rectangular shape ($3.4 \times 3.54 \times 0.57 \text{ cm}^3$) and weighed 46.35 gm. It was made with several enriched ^{90}Zr metallic foils (about $3.4 \times 3.54 \text{ cm}^2$) and thicknesses of 390 and 260 mg/cm^2 . The foils were 97.7% enriched in ^{90}Zr , about 1% ^{91}Zr ,

and about equal amounts ($\sim 0.5\%$) of ^{92}Zr and ^{94}Zr .

The neutron flux incident on the scatterer was measured by rotating the beam swinger to zero degrees with no sample-in position. With this procedure, only relative efficiencies are needed for the sevenfold array neutron detector.

Several corrections were made to the data. The source anisotropy correction was less than 3%. The dead time corrections were less than 1%. The Monte Carlo code MULCAT (Ref. 16) was used to calculate multiple-scattering, finite-size, and flux attenuation corrections. Since this code cannot handle a rectangular geometry, a sample with equivalent cylindrical geometry (to keep the same volume) was used. We tested this procedure by taking data with two graphite samples of the same height but one having the same rectangular dimensions as those of the ^{90}Zr sample and the other having a cylindrical shape. The same code MULCAT was used, handling the rectangular geometry in the same way as it was done for the ^{90}Zr sample. Computed differential cross sections, after being corrected for multiple-scattering separately for the rectangular and cylindrical shapes of graphite samples, showed an agreement within 5%. This method has been used previously¹⁷ with equal agreement.

The uncertainties in the final corrected data, especially near minima of the differential cross sections, are larger because of the assumptions used in the shape of the sample. We have accordingly increased at these minima data points the uncertainties to about 20%.¹⁵ At other angles, the uncertainty is typically 5–7%, as determined by the statistics, systematic uncertainties, and the above corrections.

III. OPTICAL MODEL ANALYSES

The data set which we use to perform the OMP analyses consists of neutron elastic scattering differential cross sections between 1.8 and 24 MeV, neutron total cross sections σ_T , for ^{90}Zr for neutron energies between 0.9 and 5.5 MeV (Ref. 7) and 0.5–2.4 MeV,⁸ total neutron cross section for $^{\text{nat}}\text{Zr}$ in the energy range from 47 keV to 20 MeV,¹¹ by Peterson *et al.*¹⁸ in the energy range from 17.4 to 28.9 MeV, and the neutron total cross section for $^{\text{nat}}\text{Mo}$ in the energy range 2.0 to 81 MeV reported by Larson.¹⁹ We have also used the *S*- and *P*-wave strength function values (S_0 and S_1) and potential scattering radius (R').¹³ A compilation of neutron total cross section data is presented in Ref. 20. No analyzing power measurements have been reported for neutron elastic scattering from ^{90}Zr . We use the spin-orbit parameter results obtained by Honoré *et al.*²¹ in their OMP analysis of differential cross sections and analyzing powers for neutron elastic scattering from ^{89}Y between 8 and 17 MeV. A total of 21 elastic neutron angular distribution data sets were used: those reported by the Argonne National Laboratory group⁷ at neutron energies between 1.8 and 4.0 MeV at energy intervals of about 0.2 MeV, by Stooksberry *et al.*⁸ at 2.1 and 5.2 MeV, by Tanaka and Yamanouti¹⁰ at 5.90, 6.92, and 7.75 MeV, the present data at 8, 10, and 24 MeV, and previously published Ohio University data at 11 MeV.⁹ All of the fitting was done

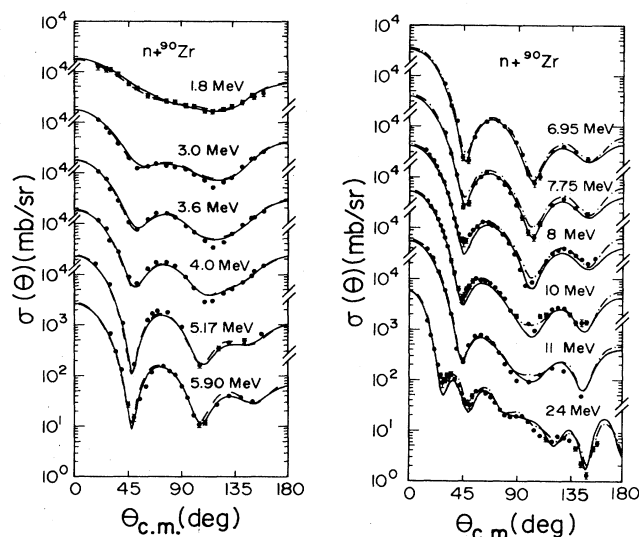


FIG. 1. Comparisons between the measured neutron elastic differential scattering cross sections and our model calculations. The dashed curves represent calculations based on grid searches while continuous curves are obtained from the dispersive approach (see text, Sec. III). Compound nucleus contributions have been added to the direct reaction predictions for incident energies up to 8 MeV. The $\sigma(\theta)$ data are from Refs. 7–10 and from the present work.

using the optical/statistical model search code OPSTAT.²² Compound nucleus contributions to the cross sections are calculated using the Hauser-Feshbach²³ theory with optional width fluctuation corrections, as modified by Moldauer.²⁴ For neutron energies larger than 8 MeV, the compound elastic contributions can be neglected. A subset of the experimental neutron elastic differential cross-section data are presented in Fig. 1.

To establish our notation, we define the empirical neutron OMP as a sum of a central potential and a spin-orbit potential. The latter is taken equal to

$$V_{\text{SO}}(r, E) = \left[\frac{\hbar}{m_{\pi} c} \right]^2 V_{\text{SO}}(E) \frac{1}{r} \frac{d}{dr} f(r, R_{\text{SO}}, a_{\text{SO}}) \mathbf{L} \cdot \boldsymbol{\sigma} ,$$

with $f(r, R_{\text{SO}}, a_{\text{SO}})$ to be of a Woods-Saxon form. We adopt throughout the present paper the parameters obtained by Honoré *et al.*²¹

$$V_{\text{SO}}(E) = 6.84 - 0.033E \text{ (MeV)} ,$$

$$r_{\text{SO}} = 1.14 \text{ fm} ,$$

and

$$a_{\text{SO}} = 0.50 \text{ fm} ,$$

and we, therefore, no longer refer to this potential in this section.

The central potential is defined as a sum of a real and absorptive terms:

$$\begin{aligned}
 U(r, E) = & -V(E)f(r, R_V, a_V) \\
 & + 4ia_D W_D(E) \frac{d}{dr} f(r, R_D, a_D) \\
 & - iW_V(E)f(r, R_W, a_W), \quad (1)
 \end{aligned}$$

where

$$f(r, R_i, a_i) = \left[1 + \exp \left[\frac{r - R_i}{a_i} \right] \right]^{-1}$$

is a Woods-Saxon form factor with $R_i = r_i A^{1/3}$.

We have conducted individual best chi-square (χ^2) fits to the data by searching on all seven central parameters for the OMP (i.e., V , r_V , a_V , W_D , r_D , a_D , W_V). Initial parameter values were taken from the neutron global OMP reported in Ref. 25. We have assumed that the geometrical parameters for the volume absorption, W_V , are equal to those for the surface absorption, W_D . Individual best fit searches for the elastic scattering cross sections indicate a preference for $W_V = 0$ at energies below 11 MeV and a small value ($W_V < 1$ MeV) at 24 MeV. We present in Fig. 2 values obtained for the other six OMP parameters as a function of neutron energy. Numerical values are available from authors. It is clear from this figure that, in general, the obtained OMP parameters do not vary smoothly with neutron energy. There is, however, a tendency for V and especially r_V to decrease as the incident neutron energy increases. We have conducted grid

searches on the OMP parameters, to obtain functional representations with smooth energy dependences.

A. Grid search analysis

At each energy for which neutron elastic differential cross section and neutron total cross section data are available, we have conducted a best χ^2 fit by searching on potential depths (V , W_D , and W_V) assuming OMP geometrical parameter values which were optimized at each energy under the following assumptions.

(1) Real central potential radius r_V . As suggested from Fig. 2, its value depends upon E . At very low incident energy, our initial guess for r_V is about 1.25 fm, while at $E = 24$ MeV the value is $r_V = 1.19$ fm. As E increases, r_V reaches an asymptotic guess value, $r_V \sim 1.18$ fm, which is similar to that adopted in Ref. 3 for the asymptotic radius of the real central potential for the n -⁴⁰Ca system.

(2) Real central potential diffuseness a_V . Sensitivity tests show that this parameter is not of central importance to fit the angular distributions and that it can be held equal to a constant value in the 0.63–0.70 fm range (Fig. 2).

(3) Absorptive potential radius r_D and diffuseness a_D . Our initial guesses for the r_D and a_D values are 1.26 and 0.58 fm, respectively. These values were obtained in extensive OMP analyses²⁶ of nucleon scattering and reaction cross sections for ⁹³Nb for incident energies for 10

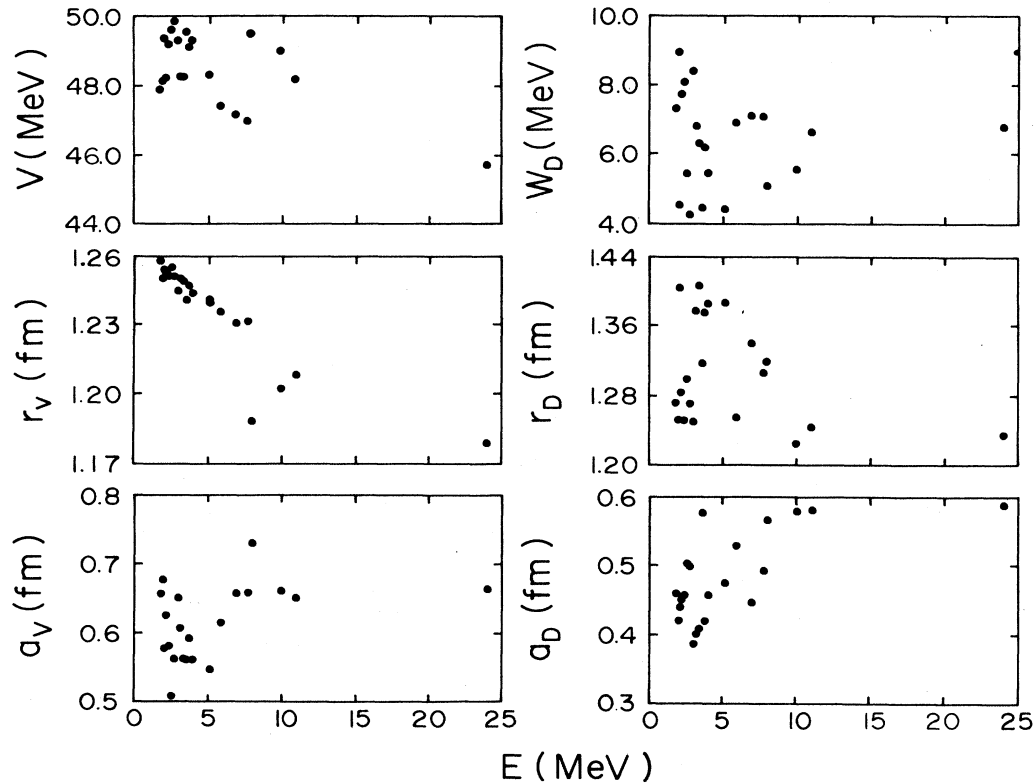


FIG. 2. Geometrical parameters and potential depths of the OMP for $n + {}^{90}\text{Zr}$ as determined from individual best χ^2 fit searches in the interval $1.8 \text{ MeV} < E < 24 \text{ MeV}$.

keV up to 50 MeV. In our work, the optimum r_D and a_D values are sought for the intervals (1.24–1.30) fm and (0.50–0.60) fm, respectively, and kept constant.

It also seems apparent from Fig. 2 that for $E < 10$ MeV the r_D values decrease with increasing energy while the a_D values increase. These energy dependences in the shape of the surface absorptive component of neutron optical potentials have been attributed to l dependences of the imaginary part of the empirical OMP, recently discussed by Johnson and Winters.²⁷

(4) Volume absorptive potential. Even though individual χ^2 searches for $0 < E < 24$ MeV suggest that W_V be small, it is indeed included in our analysis. Its geometry is usually assumed to be energy independent and equal to that used for the surface absorption term. However, and in the spirit of DR analysis, we follow the suggestion of Johnson *et al.*² and use $r_W = r_V$ and $a_W = a_V$. We use the values $r_W = 1.18$ fm and $a_W = 0.665$ fm obtained in the individual best fit analysis at $E_n = 24$ MeV.

During the numerous individual OMP calculations involved in the grid searches, the experimental values¹³ of the potential scattering radius R' as well as the S - and P -wave strength functions S_0 and S_1 are used as additional constraints placed on the OM potential in the keV energy range. In particular, these data are useful to fix the surface absorption $W_D(E)$ at very low energy and help to decide which functional representation of W_D vs E should be adopted.

The results of our grid searches performed with the code OPSTAT (Ref. 22) may be summarized as follows.

(i) Real central potential geometry. The variation of r_V vs E has tentatively been given a simple functional form:

$$r_V(E) = r_0 - r_1 \frac{E^2}{E^2 + b^2}, \quad (2)$$

where r_0 , r_1 , and b are parameters to be optimized using the $r_V(E)$ individual values. Equation (2) simulates forms obtained for $r_V(E)$ at positive energies using the iterative moment method.^{4–6}

We obtain values $r_0 = 1.24$ fm, $r_1 = 0.06$ fm, and $b = 12$ MeV. We also obtain $a_V = 0.65$ fm.

(ii) Absorptive potential geometries. The following values were obtained:

$$r_D = 1.24 \text{ fm}, \quad a_D = 0.58 \text{ fm}.$$

As indicated above in (4), we choose $r_W = 1.18$ fm and $a_W = 0.665$ fm.

(iii) Low-energy average properties. Our calculations performed at 10 keV for R' , S_0 , and S_1 resulted in values

$$R' = 6.80 \text{ fm}, \quad S_0 = 0.53 \times 10^{-4}, \quad S_1 = 3.40 \times 10^{-4},$$

which compare very well with the experimental values

$$R' = (7.1 \pm 0.35) \text{ fm}, \quad S_0 = (0.56 \pm 0.2) 10^{-4},$$

$$S_1 = (3.8 \pm 1.0) 10^{-4},$$

obtained by Boldeman *et al.*¹³

(iv) Potential depths values. We present in Fig. 3 the values obtained for the real V and absorptive (W_D, W_V) potential depths as a function of neutron energy. The

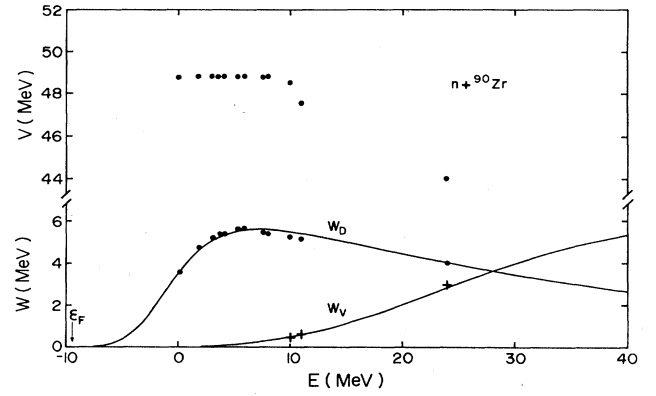


FIG. 3. Depths of the real volume (V) and imaginary surface (W_D) and volume (W_V) potentials as obtained from grid searches. The continuous curves shown for the absorptive potentials are functional representations defined in Eq. (4).

searched values for the real potential depth, $V(E)$, (Fig. 3) are nearly constant for incident neutron energies less than approximately 10 MeV, and then the values decrease rapidly. On the other hand, the depth of the surface absorption displays a more familiar E dependence: $W_D(E)$ increases to reach a plateau at around $E = 6$ MeV and then decreases smoothly with energy. The volume absorption $W_V(E)$ is small everywhere except at 24 MeV where W_V is given a value equal to 2.9 MeV. If $W_V(E)$ were to be represented as a linear function of energy, the parametrizations would be

$$W_V(E) = 0.17(E - 7) \text{ MeV} \quad (7 < E < 30 \text{ MeV}) \quad (3)$$

which seems to be a reasonable estimate.

The OMP parameters obtained in our grid searches are used to calculate the elastic differential cross sections which are shown with dashed lines in Fig. 1. There is an overall good agreement between the data and the present OMP calculations which, up to 8 MeV, combine the OMP and compound nucleus components. The agreement is of similar quality for the neutron total cross section σ_T at energies where scattering cross sections are available. Predictions for σ_T have also been made at other energies between 12 and 29 MeV and between 0.5 and 1.8 MeV to further test our OMP modeling. These have been performed by linear interpolation through the grid searched W_V and W_D values shown as dots and crosses in Fig. 3. Our predictions for the total cross section, shown as a dashed curve in Fig. 4, are in good overall agreement with the measurements in the interval from 0.5 to 29 MeV. However, they are systematically low in the 8–29 MeV range.

It is useful to represent the variations of the potential depth W_D and W_V with energy in functional forms suitable for the dispersion relation optical model analysis (see Sec. III B). After a few trials and following the schematic model of Jeukenne and Mahaux,²⁸ it is found that the best forms are

$$W_D(E) = c_1 \frac{(E - E_F)^4}{(E - E_F)^4 + d^4} e^{-gE} \text{ (MeV)} \quad (4a)$$

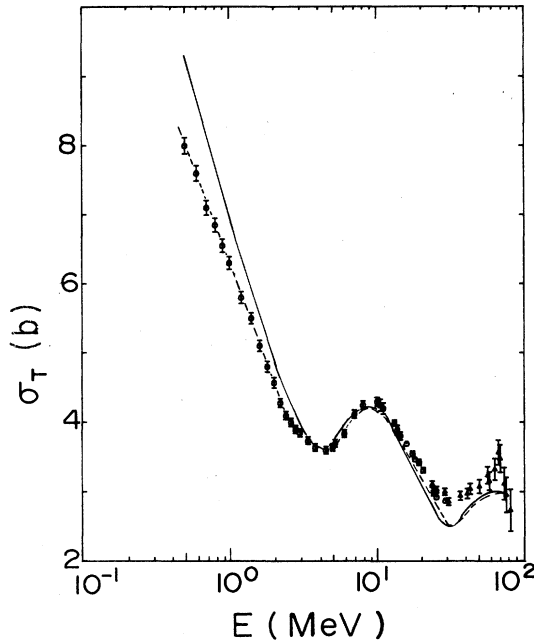


FIG. 4. Experimental neutron total cross-section values, σ_T , for ⁹⁰Zr in the energy range $0.9 < E < 5.5$ MeV (Ref. 7), for ^{nat}Zr up to 20 MeV (Ref. 11) and in the energy range $17.4 < E < 28.9$ MeV (Ref. 18). For completeness, σ_T values reported for $n + \text{natMo}$ in the energy range up to 81 MeV are shown as solid data points. The calculations for σ_T (⁹⁰Zr) are shown as a dashed line (grid search) and a solid line (dispersive OMP approach).

and

$$W_V(E) = c_2 \frac{(E - E_F)^4}{(E - E_F)^4 + h^4} \quad (\text{MeV}), \quad (4b)$$

where E_F is the Fermi energy ($E_F = -9.6$ MeV for ⁹⁰Zr).

The solid curves for W_D and W_V shown in Fig. 3 reproduce quite well the values obtained in the grid searches. They are obtained with

$$c_1 = 7.564 \text{ MeV}, \quad d = 10.0 \text{ MeV}, \quad g = 0.026 \text{ MeV}^{-1},$$

and

$$c_2 = 7.0 \text{ MeV}, \quad h = 37.0 \text{ MeV}.$$

The parameters c_2 and h for $W_V(E)$ are optimized such that the volume integral of the total absorptive potential reaches a plateau for E near 100 MeV.

B. Dispersive OMP analysis

The consequence of causality is that there exists a relationship between the real and imaginary central parts of the OMP. This relationship may be used to write the real part of the central neutron-⁹⁰Zr mean field $V(r, E)$ as the sum of a Hartree-Fock component $\mathcal{V}_{\text{HF}}(r, E)$, plus a dispersive component. The latter is determined from the absorptive part of the optical potential which connects these quantities. Thus, the real central part of the mean-

field potential is usually written²⁹

$$V(r, E) = \mathcal{V}_{\text{HF}}(r, E) + \frac{P}{\pi} \int_{-\infty}^{+\infty} \frac{W(r, E')}{E' - E} dE', \quad (6)$$

where P denotes principal value, and $W(r, E')$ the absorptive potential evaluated at energy E' . $\mathcal{V}_{\text{HF}}(r, E)$ represents the local equivalent of the nonlocal energy-independent Hartree-Fock component of the nuclear mean field, which we denote as $\mathcal{V}_{\text{HF}}(r, r')$.

With the assumption that²⁹ $W(r, E')$ be symmetric with respect to the Fermi energy E_F , Eq. (6) is expressed

$$V(r, E) = \mathcal{V}_{\text{HF}}(r, E) + \Delta V(r, E), \quad (7)$$

where

$$\Delta V(r, E) = \frac{2}{\pi} (E - E_F) P \int_{E_F}^{+\infty} \frac{W(r, E')}{(E' - E_F)^2 - (E - E_F)^2} dE', \quad (8)$$

is skew symmetric²⁹ around E_F , that is,

$$\Delta V(r, E_F + E) = -\Delta V(r, E_F - E).$$

As a consequence, ΔV needs to be evaluated only for $E \geq E_F$. Also $\Delta V(r, E_F) \equiv 0$.

The dispersive term, Eq. (8), can be expressed in a form which is convenient when evaluating the principal value either on a computer or in algebraic form. Setting $x = (E - E_F)$, with $x > 0$ since $E_F < 0$ for bound nuclei, $y = (E' - E_F)$, and using the symbolic notation

$$\tilde{W}(r, z) \equiv W(r, z + E_F),$$

Eq. (8) becomes

$$\Delta V(r, E) = \frac{2}{\pi} x \int_0^{\infty} \frac{\tilde{W}(r, y) - \tilde{W}(r, x)}{(y^2 - x^2)} dy, \quad (9)$$

since

$$P \int_0^{\infty} \frac{dy}{(y^2 - x^2)} \equiv 0.$$

The dispersive term, Eq. (9), can be evaluated for any value of the incident energy provided that $\tilde{W}(r, y)$ and its first derivative be continuous functions of y all over the interval from zero up to positive infinity. Such are the forms adopted [see Eq. (4)] for the surface and volume components of the absorption.

At this stage of the DR analysis, it is useful to make a few remarks intended to help the reader understand which potentials, together with their physical contents, are determined from empirical fits to data available at positive and negative energies. In an empirical DR approach, one tries to determine the local Hartree-Fock potential $\mathcal{V}_{\text{HF}}(r, E)$; the Hartree-Fock potential obtained in a DR analysis which we will denote as $V_{\text{HF}}(r, E)$ should, in principle, represent a good approximation to $\mathcal{V}_{\text{HF}}(r, E)$. The empirical potential $V_{\text{HF}}(r, E)$ is usually obtained at the end of a multistep procedure, as the difference between the empirical real term of the OMP, $V(r, E)$, and the dispersive term, $\Delta V(r, E)$ (Refs. 2 and 3) and is usually called the Hartree-Fock potential. The po-

tential $V(r, E)$ is directly extracted from the fits, as opposed to $\Delta V(r, E)$ which is determined through Eq. (8). Therefore, the precision attached to the $\Delta V(r, E)$ values depends upon assumptions made about the absorptive potential, among others: (i) the relation $W(r, E - E_F) = W(r, E + E_F)$, and (ii) the functional form given to $W(r, E)$ at high and low energies. The assumptions and related uncertainties propagate into the empirically determined values of $V_{\text{HF}}(r, E)$ which then might bear little resemblance with a reasonable estimate for a microscopic Hartree-Fock potential calculated with a realistic effective interaction, $\mathcal{V}_{\text{HF}}(r, E)$. Thus, the empirical potential $V(r, E) - \Delta(r, E)$ should be viewed as the smooth energy-dependent real component, $V_{\text{HF}}(r, E)$ of the empirical real term of the mean field $V(r, E)$.

We assume that the absorptive potentials have Woods-Saxon radial forms and fixed geometries as described in Sec. III A. Then the DR contributions are as follows:

$$\Delta V(r, E) = \Delta V_V(r, E) + \Delta V_D(r, E)$$

with

$$\Delta V_V(r, E) = \Delta V_V(E) f(r, R_W, a_W) \quad (10)$$

and

$$\Delta V_D(r, E) = -4a_D \Delta V_D(E) \frac{d}{dr} f(r, R_D, a_D),$$

where the values for the volume $\Delta V_V(E)$ and the surface $\Delta V_D(E)$ correction terms are calculated separately using Eq. (9).

$$U(r, E) = - \left[V_{\text{HF}}(E) f(r, R_{\text{HF}}, a_{\text{HF}}) + \Delta V_V(E) f(r, R_{\text{HF}}, a_{\text{HF}}) - 4a_D \Delta V_D(E) \frac{d}{dr} f(r, R_D, a_D) \right] + i \left[4a_D W_D(E) \frac{d}{dr} f(r, R_D, a_D) - W_V(E) f(r, R_{\text{HF}}, a_{\text{HF}}) \right]. \quad (12)$$

This form of the OMP differs from that used in the grid search analysis described in Sec. III A, mainly in that it contains a surface term, ΔV_D , in the central real potential. As such the values for potential depths obtained in the grid search are not quite correct to be used directly in Eq. (12).

A new grid search was done assuming Eq. (12) for the central OMP potential. Values for (r_D, a_D) were kept constant to the values (1.24, 0.58) fm obtained earlier. The following OMP parameters were optimized: R_{HF} , $V_V(E)$, $\Delta V_D(E)$, $W_D(E)$, and $W_V(E)$ in a grid search, where $V_V(E) = V_{\text{HF}}(E) + \Delta V_V(E)$. The value $a_V = 0.65$ fm was kept constant. Initial values for the OMP parameters were obtained from the previous grid search results. Best χ^2 values were obtained for the data set of consecutive fixed values from $r_{\text{HF}} = 1.18$ up to 1.25 fm in steps of 0.01 fm. At each stage the potential depths were optimized and the χ^2 recorded. The results indicate that the best χ^2 were obtained for energy-dependent r_{HF} values. Although the search for r_{HF} gives a shallow minima in χ^2

C. Grid search for dispersive OMP parameters

The central OMP obtained by adding the DR contributions differs slight from that given in Eq. (1). It is given by

$$U(r, E) = - \left[V(E) f(r, R_V, a_V) + \Delta V_V(E) f(r, R_W, a_W) - 4a_D \Delta V_D(E) \frac{d}{dr} f(r, R_D, a_D) \right] + i \left[4a_D W_D(E) \frac{d}{dr} f(r, R_D, a_D) - W_V(E) f(r, R_W, a_W) \right]. \quad (11)$$

In this equation we then define the Hartree-Fock component as the first term in the real part of the OMP

$$V(E) f(r, R_V, a_V) = V_{\text{HF}}(E) f(r, R_{\text{HF}}, a_{\text{HF}}).$$

This Hartree-Fock contribution to the mean field then represents the approximation that throughout the elastic scattering the target nucleus remains in its ground state and that nucleon-nucleon correlations in the ground-state wave function are neglected.

For convenience, we follow the suggestion of Johnson *et al.*² and use $r_W = r_{\text{HF}}$, $a_W = a_{\text{HF}}$ so that the volume dispersion contribution ΔV_V has the same Woods-Saxon geometrical parameters as the Hartree-Fock term.

Then the central dispersive OMP is given by

space, below 9 MeV it prefers $1.18 \leq r_{\text{HF}} \leq 1.21$ fm, while the 10–11 MeV data sets indicate a best χ^2 for $1.21 \leq r_{\text{HF}} \leq 1.24$ fm. The 24 MeV elastic scattering data and total cross section data above 15 MeV are better fitted with $1.20 \leq r_{\text{HF}} \leq 1.24$ fm. In a study of the p -⁴⁰Ca and n -⁴⁰Ca mean fields from the iterative moment approach, Mahaux and Sartor³⁰ obtain Woods-Saxon OMP parameters which also indicate energy-dependent r_{HF} values increasing with increasing energy.

Based on the χ^2 results we adopt $r_{\text{HF}} = 1.21$ fm and with this constraint we optimize all potential depths values. The searched $W_D(E)$ and $W_V(E)$ values are then fitted with expressions given in Eq. (4), and the following parameters are obtained:

$$c_1 = 7.98 \text{ MeV}, \quad d = 10 \text{ MeV}, \quad g = 0.026 \text{ MeV}^{-1}, \\ c_2 = 6.5 \text{ MeV}, \quad h = 50 \text{ MeV}.$$

These parameters differ only slightly from the previous grid search values.

We show in Fig. 5 the curves corresponding to $W_D(E)$ and $W_V(E)$ with the resulting $\Delta V_V(E)$ and $\Delta V_D(E)$ values as functions of energy between -60 and $+80$ MeV. It should be noted that the value of the DR correction term $\Delta V_D(E)$ crosses zero at $E=9.3$ MeV. At this energy value and using Eq. (2), we get $r_V(E=9.3)=1.217$ fm. This procedure has been suggested^{3,4} to choose the value for r_{HF} . The value $r_V=1.217$ fm is in good agreement with the adopted $r_{HF}=1.21$ fm value. The individual best fits OMP parameters obtained in the fits to the neutron elastic scattering data at 7.75, 8.0, 10.0, and 11.0 MeV give an average $r_V=1.21$ fm value also in agreement with the chosen value for r_{HF} .

Equations (4) and (10) are the basic inputs for the dispersive OMP calculations. The only unknown potential is the empirical Hartree-Fock term. Its depth $V_{HF}(E)$ is obtained by forming the difference $V_{HF}(E)=V_V(E)-\Delta V_V(E)$ where $V_V(E)$ is the depth of the volume part of the real central potential obtained from fits to the $\sigma(\theta)$ data. This procedure is straightforward since the $V_{HF}(r,E)$ and volume absorptive potentials $W_V(r,E)$ were *ab initio* assigned identical radial shapes and geometrical parameters (i.e., $r_{HF}\equiv r_W$ and

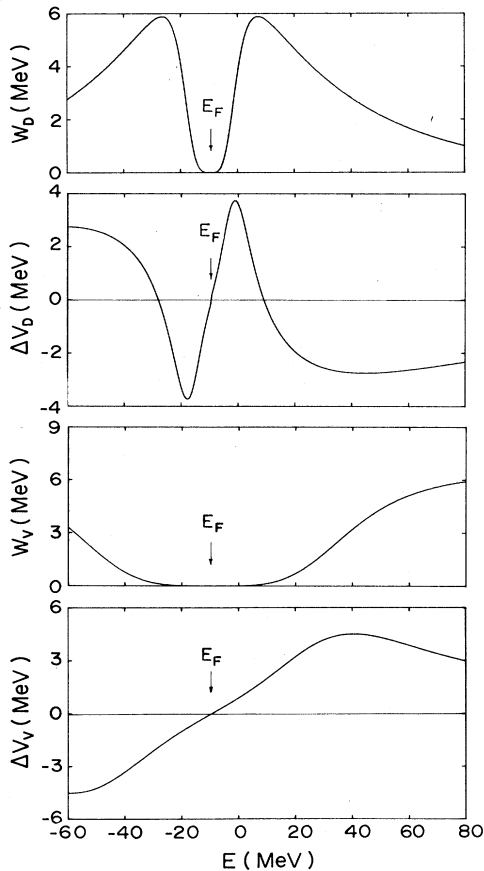


FIG. 5. The solid lines represent the surface $W_D(E)$ and volume $W_V(E)$ absorptions versus energy [see Eq. (4)] as well as the DR correction terms $\Delta V_D(E)$ and $\Delta V_V(E)$ defined through Eq. (10).

$a_{HF}\equiv a_W$). The empirical values obtained for $V_{HF}(E)$ are shown in Fig. 6. Dispersive OMP predictions for $\sigma(\theta)$ are shown as continuous curves in Fig. 1. Both dashed and continuous curves shown in this figure incorporate compound nucleus components for elastic scattering below 8 MeV. Therefore, they directly compare to the $\sigma(\theta)$ measurements. As can be seen, the overall description of the scattering data is rather good, in particular for low neutron energies. In this energy range, the phasing of $\sigma(\theta)$'s is well reproduced.

This feature is at variance with findings of Johnson *et al.*^{2,3} for $n+^{208}\text{Pb}$ and $n+^{40}\text{Ca}$ at comparable low incident neutron energies. We do not know why the phasing of the present $\sigma(\theta)$ predictions agree well with the data. A plausible explanation is that the surface absorption was carefully mapped from fits to the $\sigma(\theta)$ measurements and the low-energy average scattering and reaction parameters (R' , S_0 , and S_1).

Figure 4 shows a comparison between the neutron total cross section data for Zr and dispersive OMP calculations (continuous curve) from 0.5 up to 29 MeV. There is a good agreement between the data and the calculations except below 1 MeV where the predictions are too large. Since the σ_T predictions in this energy range almost exclusively depend upon the geometry of the real central potential, the observed disagreement probably indicates that the geometrical parameters of the complex mean field are not quite adequate in the low-energy domain. We have further tested our modeling of the complex mean field by extending the calculations for ⁹⁰Zr from 29 MeV up to 80 MeV and comparing the results with σ_T measurements available for ^{nat}Mo (Ref. 19) and represented as solid data points in Fig. 4. Both σ_T data and calculations (Fig. 4) have similar phasings and also display a maximum at around 66 MeV. However, the calculated $\sigma_T(^{90}\text{Zr})$ values are on the average 5% lower than the $\sigma_T(^{\text{nat}}\text{Mo})$ data, a shift which is also observed when com-

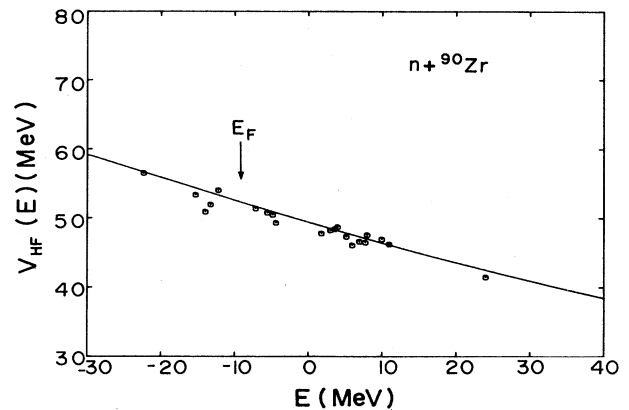


FIG. 6. Energy dependence of the depth of the empirical Hartree-Fock potential. The dots at positive energy have been obtained from the dispersive OMP analysis (Sec. III B). Those shown at negative energies (around $E_F=-9.6$ MeV) have been deduced from calculations which best describe the experimental bound state level energies. The solid line represents $V_{HF}(E)$ as defined in Eqs. (11) and (12).

paring the σ_T measurements for ^{nat}Zr and ^{nat}Mo in the 20–29 MeV range where the two data sets overlap. The comparisons shown in Fig. 4 indicate that the present assumed extrapolations beyond 29 MeV for $W_V(E)$ and $W_D(E)$ are reasonable.

IV. BOUND-STATE PROPERTIES

The most appealing facet of the dispersive OMP approach is that it offers the opportunity to obtain a shell-model potential for bound states as an extrapolation of the OMP toward negative energies. Since ^{90}Zr has often been used as a testing ground in transfer reaction measurements, a wealth of experimental information exists for the energies E_{nlj} of the single-particle states located in the vicinity of the Fermi energy. The single-particle states found immediately above and below the Fermi energy are

$$1g_{7/2}, 2d_{3/2}, 3s_{1/2}, \text{ and } 2d_{5/2} \quad (E_{nlj} > E_F)$$

and

$$1g_{9/2}, 2p_{1/2}, 2p_{3/2}, 1f_{5/2}, \text{ and } 1f_{7/2} \quad (E_{nlj} < E_F),$$

respectively. Spectroscopic information on these states may be measured by means of stripping and pickup reactions on ^{90}Zr . Graue *et al.*³¹ report on measurements of the $^{90}\text{Zr}(d,p)^{91}\text{Zr}$ reaction up to 6.5 MeV excitation energy and present neutron spectroscopic strengths and single-neutron-particle centroid energies for the $2d_{5/2}$, $2d_{3/2}$, $3s_{1/2}$, and $1g_{7/2}$ subshells. A summary of these results is presented in Table I. However, the quoted spectroscopic factors should be interpreted cautiously. The authors indicate that the quoted spectroscopic strengths for a given nlj transition have been normalized in such a way that their summed experimental strengths exhaust the expected shell-model sum rule. Kasagi *et al.*³² have studied the $^{90}\text{Zr}(p,d)$ reaction at $E_p = 90$ MeV and deduced spectroscopic information on excited neutron hole states up to 20 MeV excitation energy. Their results are

TABLE I. Empirical spectroscopic strengths and neutron single-particle centroid energies for ^{90}Zr .

nlj^c	E_{nlj} (MeV)	S_{nlj}
$1g_{7/2}$	−4.36 ^a	1.07 ^a
$3s_{1/2}$	−5.53 ^a	0.95 ^a
$2d_{3/2}$	−4.78 ^a	1.16 ^a
$2d_{5/2}$	−7.1 ^a	1.0 ^a
$1g_{9/2}$	−12.16 ^b	1.0 ^b
$2p_{1/2}$	−13.21 ^b	0.66 ^b
$2p_{3/2}$	−13.93 ^b	0.72 ^b
$1f_{5/2}$	−15.25 ^b	1.16 ^b
$1f_{7/2}$	−22.28 ^b	0.81 ^b

^aObtained from $^{90}\text{Zr}(d,p)^{91}\text{Zr}$ (Ref. 31). Uncertainty $\pm 15\%$.

^bObtained from $^{90}\text{Zr}(p,d)^{89}\text{Zr}$ (Ref. 32). Uncertainty less than 20%.

^cQuantum numbers for neutron orbitals.

also summarized in Table I. The C²S spectroscopic strengths have been normalized in such a way that the $1g_{9/2}$ strength is equal to 10 (i.e., the shell-model sum rule). In both stripping and pickup analyses some of the neutron strength may have been missed due to the fact that some of the weak transitions are not clearly observed. The empirical strength for each nlj transition (usually fragmented in many states) is used to calculate the single-particle energy positions. If the total empirical strength for a subshell with quantum numbers nlj is less than the sum rule strength, the deduced nlj single-particle energy is not properly determined. The E_{nlj} values in Table I assume that the sum rule strength for each nlj neutron orbit has been fulfilled.

It should also be mentioned that the spectroscopic factors extracted from single-particle transfer reactions are rather sensitive to the geometrical potential parameters (r_0 and a) used to describe the single-particle transfer. Because these parameters and other experimental uncertainties are not well known, papers describing single-particle transfer reactions generally quote spectroscopic strengths normalized to sum rule strengths. This practice, of course, is not justified. Realistic spectroscopic factors have been estimated only for ^{208}Pb from sub-Coulomb stripping^{33,34} and particle transfer reactions with C and O beams.³⁵ “Absolute” spectroscopic factors have been derived using radial wave functions determined from magnetic electron scattering.³⁶ No “absolute” neutron spectroscopic factors have been reported for ^{90}Zr that we can use to compare with predictions of our $n + ^{90}\text{Zr}$ mean-field calculations (see Sec. IV B 2).

The single-particle centroid energies estimated from these measurements are shown in Fig. 7 where they are compared with the results obtained with the mean-field calculations. The purpose of these calculations is twofold: (i) find the depth $V_{\text{HF}}(E)$ at $E = E_F$ so that the calculated single-particle centroid energies for the last occupied single-particle level ($1g_{9/2}$) and for the first unoccupied single-particle level ($2d_{5/2}$) be symmetric around the Fermi energy,³⁷ and (ii) evaluate the validity of the dispersive OMP analysis when extrapolating the OMP parameters toward negative energies.

A. Single-particle energies

The single-particle energy calculations are performed using a subroutine implemented in the distorted wave code DWUCK4 [Ref. 38], and following a trial-error method in which $V_{\text{HF}}(E)$ is given the functional form²

$$V_{\text{HF}}(E) = V_{\text{HF}}(E_F) \exp[-\alpha(E - E_F)/V_{\text{HF}}(E_F)]. \quad (13)$$

In this procedure, an initial value E_0 is guessed for E (considered here as a dummy parameter) to evaluate $V_{\text{HF}}(E_0)$, $\Delta V_V(E_0)$, and $\Delta V_D(E_0)$ through Eqs. (10) and (13) and to solve the bound-state problem. Let us call $E_{nlj}^{(0)}(E_0)$ this eigenvalue and form the quantity

$$\Delta_{nlj}^{(0)} = E_{nlj}^{(0)}(E_0) - E_0.$$

Then, another value E_1 is chosen to evaluate $V_{\text{HF}}(E_1)$,

$\Delta V_V(E_1)$, and $\Delta V_D(E_1)$ and calculate $E_{nlj}^{(1)}(E_1)$, etc. Finally, a proper eigenvalue is obtained after m iterations where $\Delta_{nlj}^{(m)}$ reaches zero. In practice, we have considered that a calculated single-particle energy is an eigenvalue of the bound-state problems when

$$|\Delta_{nlj}^{(m)}| \leq 10 \text{ keV} .$$

All the bound-state calculations are performed using the same spin-orbit potential parameters of Sec. III except that we choose the depth of this potential to be constant and equal to $V_{SO}(E=0)=6.84 \text{ MeV}$. The values adopted for the parameters $V_{HF}(E_F)$ and α entering Eq. (13), namely,

$$V_{HF}(E_F)=52.45 \text{ MeV}$$

and

$$\alpha=0.33 ,$$

also lead to a reasonable representation of the empirical V_{HF} values found earlier in the dispersive OM analysis, as shown in Fig. 6.

The single-particle energies calculated with the real

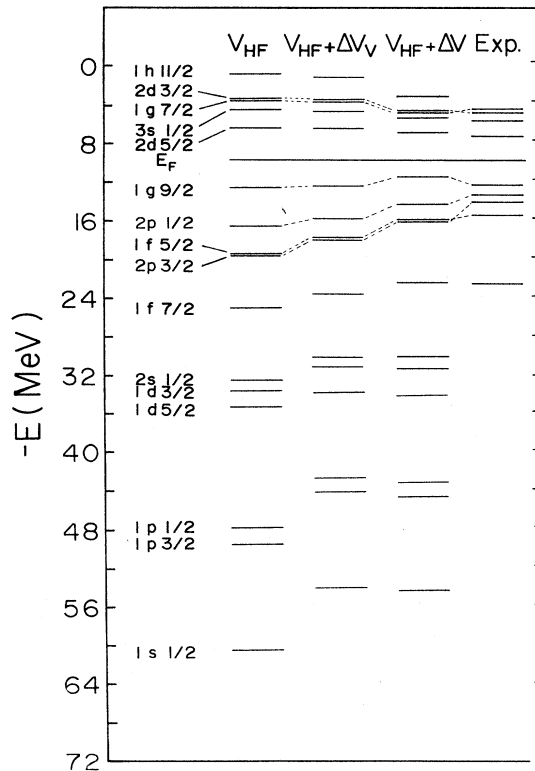


FIG. 7. Neutron single-particle energies E_{nlj} in ⁹⁰Zr. The first column at the left gives the calculated values obtained with the empirical V_{HF} potential of Sec. III. The second column are those calculated with the addition to V_{HF} of the volume DR contribution, while the third column are those with the mean field potential $V_{HF}+\Delta V$. The column labeled EXP contains experimental values from Ref. 31 in the case of particle states and from Ref. 32 for hole states.

term of the mean field

$$V(r, E)=V_{HF}(r, E)+\Delta V_V(r, E)+\Delta V_D(r, E)$$

are shown in the third column of Fig. 7 and in Table II, where they are compared with the empirical values from Table I. There is a good agreement between the experimental and calculated single-particle energies except that the ordering of the predicted $2d_{3/2}$ and $1g_{7/2}$ levels do not follow the experimental pattern.

The bound-state calculations have been extended down below the Fermi energy. In this energy domain, the real term of the mean field with an exponential parametrization for $V_{HF}(E)$, Eq. (11), is expected^{2,3} to produce overbound hole states. For this reason, we adopt a linear E dependence for $V_{HF}(E)$ in the region $E < E_F$, namely,

$$V_{HF}(E)=V_{HF}(E_F)-\gamma(E-E_F) \quad (14)$$

with

$$\gamma=0.33 .$$

The hole states energies calculated with the real term of the mean field in which $V_{HF}(E)$ is given by Eq. (14) are shown in the third column of Fig. 7 and in Table II. The sequential ordering of these single-particle levels agree with the experimental data, but the predicted single-particle levels are slightly tightly bound (with exception for the $1g_{9/2}$ hole level).

Single-particle energy predictions calculated with just $V_{HF}(r, E)$ are shown in the first column of Fig. 7, while in the second column are shown the values calculated with the addition of the volume DR contribution,

TABLE II. Neutron single-particle energies E_{nlj} in ⁹⁰Zr. Each state is characterized by the principal n , orbital l , and total angular momentum j , quantum numbers. The second through fourth columns contain the predicted values obtained in Sec. III from the Hartree-Fock field alone, the HF plus the volume dispersive term and the real term of the mean-field potential, respectively. The last column contains the empirical values from Table I.

nlj	V_{HF}	$V_{HF}+\Delta V_V$	$V_{HF}+\Delta V$	E_{exp} (MeV)
1h _{11/2}	-0.90	-1.19	-3.30	
1g _{7/2}	-3.61	-3.81	-5.04	-4.36
2d _{3/2}	-3.50	-3.68	-4.84	-4.78
3s _{1/2}	-4.64	-4.74	-5.59	-5.53
2d _{5/2}	-6.56	-6.53	-7.14	-7.10
1g _{9/2}	-12.58	-12.36	-11.62	-12.16
2p _{1/2}	-16.29	-15.76	-14.4	-13.21
2p _{3/2}	-18.62	-17.93	-16.18	-13.93
1f _{5/2}	-18.44	-17.64	-16.14	-15.25
1f _{7/2}	-24.95	-23.49	-22.49	-22.28
2s _{1/2}	-32.31	-29.93	-30.05	
1d _{3/2}	-33.68	-30.96	-31.21	
1d _{5/2}	-37.32	-34.14	-34.58	
1p _{1/2}	-47.82	-43.04	-43.53	
1p _{3/2}	-49.31	-44.32	-44.94	
1s _{1/2}	-60.40	-54.15	-54.52	

$V_{\text{HF}}(r, E) + \Delta V_V(r, E)$. Comparing these calculations with those obtained using the real part of the mean field, one sees that the nuclear dynamics compresses the energy of the single-particle levels around the Fermi energy, a feature already observed in similar studies^{3,2} for ^{40}Ca and ^{208}Pb . The nuclear dynamics simulated by the DR correction not only appears for valence orbits but also propagate across the major shells.

We have also compared the single-particle energy predictions calculated with $V_{\text{HF}}(r, E)$ with predictions from Hartree-Fock calculations performed using the finite range density-dependent force of Gogny.³⁹ The two sets of single-particle energy predictions agree remarkably well both for particle as well as for hole states.

B. Other bound-state properties

To complete our analysis, we have used the empirical mean-field potential to calculate other properties of bound states and present a comparison with available empirical results. Similar analyses are presented in Refs. 2 and 3 for the $n + ^{208}\text{Pb}$ and $n + ^{40}\text{Ca}$ studies. The distorted wave code DWUCK4 (Ref. 38) was used to calculate properly normalized radial wave functions, defined as $\bar{U}_{nlj}(r)$ in Ref. 1, to a radius r of 20 fm.

1. Occupation probabilities

We use the equations of Refs. 1 and 2 for occupation probability, N_{nlj} , of the single-particle state (n, l, j) defined as either

$$N_{nlj} = \int_{E_F}^{\infty} \bar{U}_{nlj}^2(r) \left[1 + \pi^{-1} \int_{E_F}^{\infty} \frac{W(r, E')}{(E' - E_{nlj})^2} dE' \right] dr, \quad E_{nlj} < E_F \quad (15)$$

for hole states, or

$$N_{nlj} = - \int_0^{\infty} \bar{U}_{nlj}^2(r) \left[\pi^{-1} \int_{-\infty}^{E_F} \frac{W(r, E')}{(E' - E_{nlj})^2} dE' \right] dr, \quad E_{nlj} > E_F \quad (16)$$

in the case of a particle state. The calculated occupation probabilities are listed in Table III. In the valence orbits, we calculate 11.5 neutrons, 8.9 of which are in the $1g_{9/2}$ subshell and 2.6 above the Fermi energy. The total number of neutrons in the valence orbits differs from 10 because the depletion of the shells below the Fermi energy in part feed orbits which lie in the continuum. The calculated total number of neutrons in all orbits is 49.7, not exactly 50 probably because of approximations.

The calculated occupation number of neutrons in the $1g_{9/2}$ subshell is 0.89. It is interesting to note that in the $^{90}\text{Zr}(d, p)^{91}\text{Zr}$ reaction the $\frac{9}{2}^+$ state in ^{91}Zr at 2.13 MeV is weakly populated.³¹ It would be interesting to estimate the possible $l = 4$ strength to determine the actual occupancy of the neutron $1g_{9/2}$ subshell.

The occupation probabilities of each orbital (n, l, j) are also shown as dots in Fig. 8. By drawing continuous curves through the N_{nlj} 's separately at $E < E_F$ and

TABLE III. Bound-state properties. Calculated values using the mean field of Sec. III for levels characterized by the nlj quantum numbers. Neutron single-particle energies E_{nlj} , rms radius R_{nlj}^{rms} , occupation probabilities, and absolute spectroscopic factors S_{nlj} are presented.

nlj	E_{nlj} (MeV)	R_{nlj}^{rms} (fm)	N_{nlj}	S_{nlj}
$1h_{11/2}$	-3.28	5.21	0.080	0.75
$1g_{7/2}$	-5.04	4.84	0.083	0.75
$2d_{3/2}$	-4.84	5.33	0.072	0.78
$3s_{1/2}$	-5.59	5.44	0.068	0.80
$2d_{5/2}$	-7.10	5.04	0.088	0.80
$1g_{9/2}$	-11.62	4.74	0.89	0.77
$2p_{1/2}$	-14.40	4.31	0.93	0.78
$2p_{3/2}$	-16.18	4.26	0.93	0.84
$1f_{5/2}$	-16.14	4.17	0.94	0.85
$1f_{7/2}$	-22.49	4.32	0.95	0.99
$2s_{1/2}$	-30.05	3.74	0.96	0.99
$1d_{3/2}$	-31.21	3.84	0.97	0.96
$1d_{5/2}$	-34.58	3.97	0.97	0.95
$1p_{1/2}$	-43.53	3.42	0.97	0.93
$1p_{3/2}$	-44.94	3.51	0.98	0.93
$1s_{1/2}$	-54.52	2.88	0.97	0.98

$E > E_F$ and extrapolating these curves to $E = E_F - \eta$ and $E = E_F + \eta$, respectively, with η as an arbitrarily small positive number, the magnitude of the discontinuity, Z , at $E = E_F$ is $Z \sim 0.76$ (Fig. 8). Since $1/Z$ is a measure⁴⁰ of the E mass defined in Ref. 2 as

$$\bar{m}/m(r, E) = 1 - \frac{d}{dE} \Delta V(r, E),$$

it is interesting to compare the value $1/Z = 1.35$ with \bar{m}/m evaluated at $E = E_F$. A plot of \bar{m}/m at this energy is shown in Fig. 9 together with the K mass (m_H^*/m) and the total mass (m^*/m) of the mean field, as defined in Ref. 2. It can be seen that the value of $1/Z$ compares well with the E mass if \bar{m}/m is evaluated at a radius value near the surface (Fig. 9).

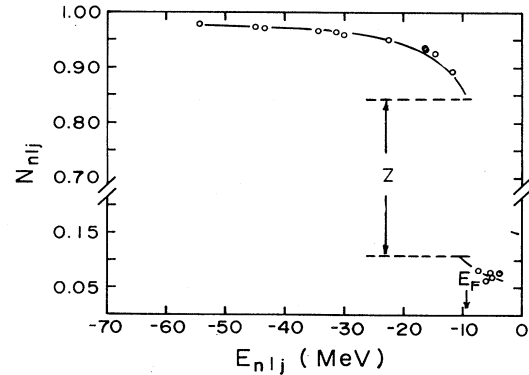


FIG. 8. Values for the occupation probability N_{nlj} vs single-particle energies. The dots represent the N_{nlj} values shown in Table III. The continuous curves are just drawn to guide the eye. Z measures the gap between the two continuous curves at the Fermi energy.

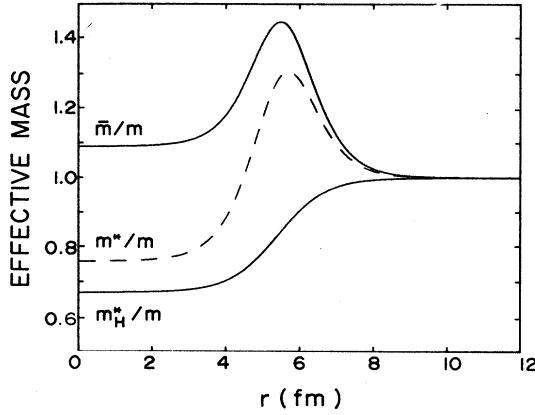


FIG. 9. Radial dependence of the effective masses \bar{m}/m , m^*/m and m_H^*/m evaluated at the Fermi energy ($E_F = -9.6$ MeV).

2. Spectroscopic factors

The spectroscopic factor is given by the following expression:^{1,5}

$$S_{nlj} = \int_0^\infty \bar{U}_{nlj}^2(r) [m/\bar{m}(r, E_{nlj})] dr, \quad (17)$$

where

$$\bar{m}(r, E_{nlj})/m = 1 - \left. \frac{d}{dE} \Delta V(r, E) \right|_{E=E_{nlj}}.$$

These calculated values are listed in Table III and should be compared with the “absolute” spectroscopic factors.³⁶ No empirical values have been obtained.

3. The rms radius of valence orbits

The rms radius for each nlj is evaluated by using the expression²

$$R_{nlj}^{\text{rms}} = \left[\int_0^\infty \bar{U}_{nlj}^2(r) r^2 dr \right]^{1/2}. \quad (18)$$

The results are listed in Table III. These values must wait for measurements such as those described in Ref. 36 for critical evaluation.

4. Energy dependence of radial moments

The volume integral or zeroth moment,

$$J_V/A = \frac{4\pi}{A} \int r^2 V(r, E) dr,$$

and the rms radius $R_{\text{rms}} = \langle r_V^2 \rangle^{1/2}$ or the normalized second moment of the radial distribution:

$$\langle r_V^2 \rangle = \frac{\int r^4 V(r, E) dr}{\int r^2 V(r, E) dr},$$

of the real part of the mean field are shown as continuous curves in the upper part of Fig. 10. In the same figure, we also show: (i) the moments J_V/A and R_{rms} of $V_{\text{HF}}(r, E)$ which are represented as dot-dashed curves,

and (ii) the moments deduced from experimental information shown as solid circles. At positive energies, the empirical moments are those from grid searches evaluated at $E = 0.010, 1.8, 3.0, 3.6, 4.0, 5.17, 5.90, 6.95, 7.75, 8.0, 10.0, 11.0,$ and 24 MeV. At negative energies, the moments are those of the real part of the mean field in which the depth of the HF component has been adjusted to reproduce the experimental single-particle energies. The energy dependences observed in the continuous curves for J_V/A and R_{rms} in the vicinity of the Fermi energy mainly reflect the energy dependence of $\Delta V_D(E)$ shown in Fig. 5. Similar features have also been found for the real part of the mean field of the $n + {}^{208}\text{Pb}$ and $n + {}^{40}\text{Ca}$ systems.^{2,3}

The uncertainty attached to R_{rms} deduced in the grid-search analysis ranges from 2.5% at $E \geq 8$ MeV up to 3% toward lower energies. The 2.5% estimate is inferred from model-independent analyses⁴¹ of the $\sigma(\theta)$ measurements performed at 8, 10, and 24 MeV. On the other hand, the 3% figure quoted for the lower energies results from adding in quadrature the 2.5% uncertainty with an

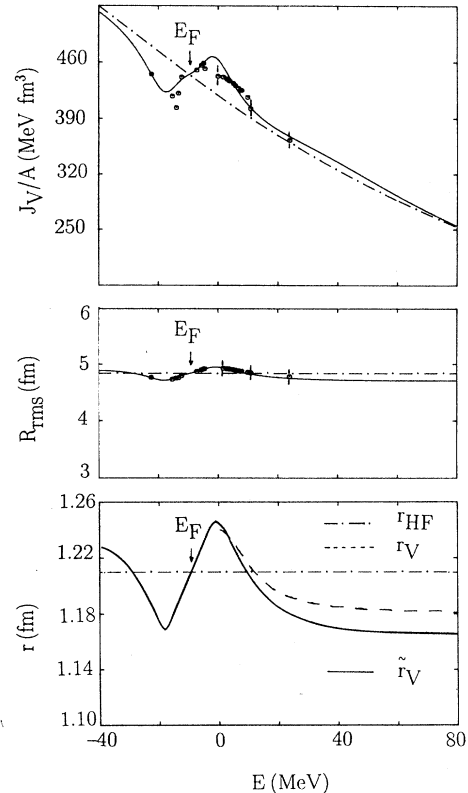


FIG. 10. Global properties of the mean-field potential. Energy dependences of the volume integral J_V/A , R_{rms} and “effective” Woods-Saxon potential radius \tilde{r}_V are shown as solid curves. The data points shown in the upper two panels represent empirical information obtained from grid searches. The dotted curve in the lower panel represents the radius $r_V(E)$, Eq. (2) of the real potential used in the grid search. The dot-dashed lines illustrate the properties of the V_{HF} potential of Sec. III.

additional uncertainty stemming from the precision with which we estimate the calculation of the compound nucleus process. With the same reasonings, the uncertainties attached to the empirically determined values of J_V/A are in the range of 3.5% at $E \geq 8$ MeV and 5% at lower energies. No uncertainties are given for the points shown in Fig. 10 at negative energies. The reason is that we do not know how precise are the values adopted for the centroid energies of the single-particle states. In this context, there is a good overall agreement between the continuous curves and the points shown in Fig. 10. Also, we notice that without experimental information at negative energies, it would have been impossible to detect the anomalous behavior of the real part of the $n + {}^{90}\text{Zr}$ mean field in the vicinity of the Fermi energy.

V. DISCUSSION

A. Mean field for $n + {}^{90}\text{Zr}$

The moments of the real part of the mean field shown as continuous curves in the upper part of Fig. 10 could be identified with the moments of an equivalent Woods-Saxon potential, with geometrical parameters \bar{r}_V and \bar{a}_V . The OMP geometrical parameters of this equivalent potential are energy dependent. If the assumption is made that $\bar{a}_V \equiv a_V = 0.65$ fm (a_V is the diffuseness of the volume potential defined in Sec. III A), then \bar{r}_V , the equivalent radius, can directly be compared with r_V , the radius of the volume potential defined in the grid search analysis (see Sec. III A).

The values of \bar{r}_V , shown as a solid curve in the lower part of Fig. 10, decrease from $\bar{r}_V = 1.245$ fm at $E = 0$ MeV down to about $\bar{r}_V = 1.17$ fm at $E = 24$ MeV. The radius $r_V(E)$ shown as a dotted curve displays a similar rapid variation in this energy interval. In the energy interval 40–80 MeV both \bar{r}_V and r_V remain almost energy independent and r_V about 1% larger than \bar{r}_V .

B. Comparison between empirical mean fields

The neutron + ${}^{40}\text{Ca}$ and neutron + ${}^{208}\text{Pb}$ empirical mean fields obtained from a dispersive optical model analysis are reported in Refs. 3 and 2, respectively. In this section we briefly compare our results for the neutron + ${}^{90}\text{Zr}$ mean field with those in Refs. 2 and 3.

The mean field obtained in these analyses consist of a dispersive contribution due to the coupling of the neutron to the excited states of the core added to a smooth energy-dependent term called $V_{\text{HF}}(r, E)$. By definition the latter component is not much influenced by the coupling of the neutron to core excitations and thus should have a smooth mass number A and neutron excess dependences. We present in Table IV Woods-Saxon geometrical parameters obtained for these phenomenological HF potentials.

In Ref. 3 the authors comment that the increase in the radius parameter r_{HF} from 1.18 fm for ${}^{40}\text{Ca}$ to 1.24 fm for ${}^{208}\text{Pb}$ reflects the dependence of the density radius upon mass number. The same dependence predicts an increase of 0.02 fm when A increases from 40 to 90. The

TABLE IV. Geometrical parameters for HF potentials and average best fit potentials. All values in fm. A Woods-Saxon radial dependence has been assumed.

	r_{HF}	a_{HF}	r_V^a	a_V^a
${}^{40}\text{Ca}$	1.18 ^b	0.70 ^b	1.15	0.75
${}^{90}\text{Zr}$	1.21	0.65	1.19	0.65
${}^{208}\text{Pb}$	1.24 ^c	0.68 ^c	1.21	0.67

^aReference 42.

^bReference 3.

^cReference 2.

$r_{\text{HF}} = 1.21$ fm value we obtained for ${}^{90}\text{Zr}$ agrees with this prediction. In Table IV we also present values for individual average geometry parameters obtained in the OMP neutron scattering analysis on the same nuclei.⁴²

The energy variation of the $V_{\text{HF}}(E)$ potential depth for energies $E > E_F$ for $n + {}^{40}\text{Ca}$ (Ref. 3), $n + {}^{90}\text{Zr}$ (this work), and $n + {}^{208}\text{Pb}$ (Ref. 2) are given by the following equations:

$$-V_{\text{HF}}^{\text{Ca}}(E) = 58.8 \exp[-0.55(E - E_F)/58.8],$$

$$E_F = -12 \text{ MeV}, \quad \epsilon = 0,$$

$$-V_{\text{HF}}^{\text{Zr}}(E) = 52.45 \exp[-0.33(E - E_F)/52.45],$$

$$E_F = -9.6 \text{ MeV}, \quad \epsilon = 0.111,$$

$$-V_{\text{HF}}^{\text{Pb}}(E) = 46.4 \exp[-0.31(E - E_F)/46.4],$$

$$E_F = -6 \text{ MeV}, \quad \epsilon = 0.212,$$

where $\epsilon = (N - Z)/A$ is the asymmetry parameter.

As noted in Ref. 3, the difference in these expressions are namely due to two reasons: (i) the central part of the neutron OMP consists of isoscalar and isovector terms, the latter being proportional to ϵ , and (ii) the central matter density tends to decrease with increasing mass number A .

Although it is convenient to measure the energies from the Fermi energy as done in the above equations, it has been traditional to express the energy dependence of parameters of the OMP as a function of the incident energy. Using a linear approximation and the respective E_F values, we get

$$-V_{\text{HF}}^{\text{Ca}}(E) \cong 52.6 - 0.55E \text{ (MeV)},$$

$$-V_{\text{HF}}^{\text{Zr}}(E) \cong 49.4 - 0.33E \text{ (MeV)},$$

$$-V_{\text{HF}}^{\text{Pb}}(E) \cong 44.6 - 0.31E \text{ (MeV)}.$$

These HF potentials may be written as an algebraic sum of isoscalar $V_{\text{HF}}^0(E)$ and isovector $V_{\text{HF}}^1(E)$ terms:

$$V_{\text{HF}}(E) = V_{\text{HF}}^0(E) - \epsilon V_{\text{HF}}^1(E).$$

If the difference between the above potential values is attributed just to $V_{\text{HF}}^1(E)$, we can use values for the Ca-Zr and Ca-Pb potentials to get an average value

$$V_{\text{HF}}^1(E) = 33.3 - 1.6E \text{ (MeV)}$$

assuming linear energy dependences $V(E) = V(0) - \alpha E$, for these potentials. The geometrical OMP values are different for each nucleus (Table IV) and thus we also have calculated the isovector volume integrals to obtain an average value

$$\frac{J_{\text{HF}}^1(E)}{A} = 476.4 - 14.8E \text{ (MeV fm}^3\text{)} .$$

Those values are larger, especially the coefficients α representing the linear energy dependence, than empirical values obtained in neutron global analyses.²⁵

If we use values for the Zr-Pb potentials, we get

$$V_{\text{HF}}^1(E) = 47.6 - 0.2E \text{ (MeV)} ,$$

$$\frac{J_{\text{HF}}^1(E)}{A} = 399.5 - 1.7E \text{ (MeV fm}^3\text{)} ,$$

which gives values for the coefficients α in good agreement with empirical values.²⁵

The isovector values obtained from the Zr-Pb potentials reflect linear energy coefficients which are almost an order of magnitude smaller than those obtained from the Zr-Ca or Pb-Ca potentials. This is attributed to the large $\alpha = 0.55$ value, obtained for $V_{\text{HF}}^{\text{Ca}}$ (Ref. 3). However, and as indicated in Ref. 3, these results should be considered just as crude estimates of the isovector potential because (a) we have neglected effects due to the variation of the central density with A , and (b) the dispersive contribution in each nucleus are different enough that it cannot be neglected in these type of comparisons.

VI. CONCLUSION

The aim of this paper is to apply the dispersive optical model approach of Mahaux *et al.* to the study of the neutron interaction in the neutron-closed-shell nucleus ⁹⁰Zr.

To make it as complete as possible, we have enlarged the existing scattering and reaction data base by performing new elastic scattering measurements at three incident energies ($E = 8, 10, \text{ and } 24 \text{ MeV}$) which are of critical importance for a proper determination of the interplay between surface and volume absorptions in the OMP analyses. A set of smoothly energy-dependent OMP parameters is obtained from grid searches, which then are used to build a dispersive OMP and its extrapolation toward negative energies. This grid search technique, which so far has never been used in the design of a nuclear mean field at positive and negative energies, is shown to be rather successful in the entire energy range where data exist. Predictions for rms radii, occupancies, and spectroscopic factors of the particle and hole states are also presented. It would be nice to see whether these predicted bound-state properties find an experimental confirmation, for instance, from deep inelastic ($e, e'n$) transitions and/or (p, pn) reactions.

ACKNOWLEDGMENTS

One of us (J.R.) would like to thank Dr. N. S. P. King from Los Alamos National Laboratory for the loan of the enriched ⁹⁰Zr foils. We are indebted to Dr. M. Girod at the Centre d'Etudes de Bruyères-le-Châtel for the Hartree-Fock calculations. We also would like to thank the National Nuclear Data Center at Brookhaven National Laboratory for providing us with neutron cross section data. One of us (J.P.D.) would like to thank the support received during his stay at Ohio University. The computational assistance provided by S. Mande is greatly appreciated. The authors also sincerely appreciate comments to the paper suggested by C. Johnson. This work was supported in part by the National Science Foundation.

*Permanent address: Centre d'Etudes de Bruyères-le-Châtel, P.O. Box 12, 91680 Bruyères-le-Châtel, France.

¹C. Mahaux and H. Ngô, Nucl. Phys. **A431**, 486 (1984); see also, C. Mahaux and R. Sartor, Workshop on The Many Facets of Nuclear Physics, Torino, Italy, 1987 (unpublished).

²C. H. Johnson, D. J. Horen, and C. Mahaux, Phys. Rev. C **36**, 2252 (1987).

³C. H. Johnson and C. Mahaux, Phys. Rev. C **38**, 2589 (1988).

⁴C. Mahaux and R. Sartor, Nucl. Phys. **A481**, 381 (1988).

⁵C. Mahaux and R. Sartor, Nucl. Phys. **A475**, 247 (1987).

⁶C. Mahaux and R. Sartor, Nucl. Phys. **A468**, 193 (1987).

⁷P. Guenther, A. B. Smith, and J. Whalen, Phys. Rev. C **12**, 1797 (1975).

⁸R. W. Stooksberry, J. H. Anderson, and M. Goldsmith, Phys. Rev. C **13**, 1061 (1976).

⁹D. E. Bainum *et al.*, Nucl. Phys. **A311**, 492 (1978).

¹⁰S. Tanaka and Y. Yamanouti, NEANDC Report No. NEANDC(J)-55/U, 1980.

¹¹W. P. Poenitz and J. F. Whalen, Argonne National Laboratory Report No. ANL/NDM-80, 1983.

¹²J. M. Peterson, A. Bratenahl, and J. P. Stoering, Phys. Rev. **120**, 521 (1960).

¹³J. W. Boldeman *et al.*, Nucl. Phys. **A246**, 1 (1975); **A269**, 31 (1976).

¹⁴R. W. Finlay *et al.*, Nucl. Instrum. Methods **198**, 197 (1982).

¹⁵Y. Wang and J. Rapaport (unpublished).

¹⁶W. E. Kinney, Nucl. Instrum. Methods **83**, 15 (1970); Ph.D. dissertation, University of Tennessee, 1968.

¹⁷R. C. Taylor *et al.*, Nucl. Phys. **A401**, 237 (1983).

¹⁸J. M. Peterson *et al.*, Phys. Rev. **120**, 521 (1960).

¹⁹D. C. Larson, Brookhaven National Laboratory Report No. BNL-NCS-51245, 1980.

²⁰D. I. Garber and R. R. Kensey, Brookhaven National Laboratory Report No. BNL-325, 1976.

²¹G. Honoré *et al.*, Phys. Rev. C **34**, 825 (1986).

²²J. R. M. Annand, R. Das, and D. Wang, code OPSTAT, Ohio University, 1985 (unpublished).

²³W. Hauser and H. Feshbach, Phys. Rev. **87**, 366 (1952).

²⁴P. A. Moldauer, Nucl. Phys. **A344**, 185 (1980).

²⁵J. Rapaport, Phys. Rep. **87**, 25 (1982).

²⁶Ch. Lagrange and A. Lejeune, Phys. Rev. C **25**, 2278 (1982).

²⁷C. H. Johnson and R. R. Winters, Phys. Rev. C **37**, 2340 (1988).

²⁸J. P. Jeukenne and C. Mahaux, Nucl. Phys. **A394**, 445 (1983).

- ²⁹C. Mahaux and H. Ngô, Nucl. Phys. **A378**, 205 (1982).
³⁰C. Mahaux and R. Sartor, Nucl. Phys. **A484**, 205 (1988).
³¹A. Graue *et al.*, Nucl. Phys. **A187**, 141 (1983).
³²J. Kasaqi *et al.*, Phys. Rev. C **28**, 1065 (1983).
³³M. Dost, W. R. Hering, and W. R. Smith, Nucl. Phys. **A93**, 357 (1967).
³⁴J. P. Schiffer and H. J. Korner, Phys. Rev. C **8**, 841 (1973).
³⁵M. A. Franey, J. S. Lilley, and W. R. Phillips, Nucl. Phys. **A324**, 173 (1979).
³⁶A. E. L. Dieperink and I. Sick, Phys. Lett. **109B**, 1 (1982).
³⁷C. Mahaux and H. Ngô, Nucl. Phys. **A378**, 205 (1982).
³⁸P. D. Kunz, code DWUCK4 (unpublished).
³⁹J. Decharge and D. Gogny, Phys. Rev. C **21**, 1568 (1980); M. Girod (private communication).
⁴⁰S. Fantoni and V. R. Pandharipande, Nucl. Phys. **A427**, 473 (1984).
⁴¹Y. Wang, Ph.D. dissertation, Ohio University, 1988.
⁴²J. Rapaport, V. Kulkarni, and R. W. Finlay, Nucl. Phys. **A330**, 15 (1979).